Dust dynamics during the plasma afterglow

Igor Denysenko, Maxime Mikikian, Nikolai Azarenkov

Dust dynamics during the plasma afterglow

I B Denysenko[1,2,3], M Mikikian[2] and N A Azarenkov[1]

[1]School of Physics and Technology, V N Karazin Kharkiv National University, Kharkiv, Ukraine
[2]GREMI, UMR7344 CNRS/Université d'Orléans, F-45067 Orléans, France
[3]Le Studium, Loire Valley Institute for Advanced Studies, Orléans & Tours, France

E-mail: idenysenko@yahoo.com

Received
Accepted for publication
Published

Abstract

The charge and dynamics of dust particles in an afterglow plasma are studied using a 1D model in the diffusion approximation, taking into account the transition from ambipolar to free diffusion. It is analyzed how external conditions (dust particle size, neutral gas pressure and initial electron density) affect the dust motion. The dust particle dynamics has been examined in microgravity conditions and in presence of gravity. Without gravity, the location of dust particles in plasma volume may change essentially during the afterglow if the dust size and pressure are small ($\leq$ 10 nm and $\leq$ 30 mTorr, respectively). At small pressures, in the very beginning of afterglow, small nanoparticles move to the plasma boundary because the ion drag force dominates over the electric force. At afterglow times when the electron temperature becomes time-independent, the ion drag force decreases faster with time than the electric force due to the ion density decrease, and dust particles may move to the slab center. In presence of gravity, the effect of gravity force on dust particles is important only at large afterglow times ($t \geq 10$ ms), when the electric and ion drag forces are small. The dust dynamics depends essentially on the initial plasma density. If the density is large (~ 10^{12} cm^{-3}), small nanoparticles ($\leq$ 10 nm) may deposit on plasma walls in the beginning of plasma afterglow because of an enhancement of the ion drag force.

Keywords: plasma, dust particles, afterglow, 1D model, dust dynamics

1. Introduction

Plasmas with nano- and micrometer- sized particles (dust particles) have shown interesting fundamental phenomena like formation of different structures (plasma crystals, dust voids and dust balls, etc.), phase transitions, clustering and wave propagation [1–5]. They have been also indispensable in the fabrication of composite materials, silicon films, ultrahard coatings, medical materials, etc.[6 – 9] Because of the basic physical and technological interest, the complex plasmas have been intensively studied in the last three decades.

Most of the existing studies on dusty plasmas, including those on dust dynamics [1, 2, 10, 11], have focused mainly on the steady-state regime. Meantime, there are also some works where the properties of dusty plasma afterglows and nonstationary dusty plasmas are analyzed [12 – 23]. In particular, an experiment on the decharging of a RF (radio frequency) dusty plasma in microgravity conditions was conducted in [12], where the time-dependence of the charge of micrometer dust particles in the temporal afterglow was analyzed both theoretically and experimentally. It was shown that the dust particles keep a negative charge for a long time in the afterglow. Dust particle residual charges in the afterglow of a dusty plasma were also measured in laboratory conditions in [13 – 15], where an upward thermophoretic force was applied to balance gravity. In [13], it was found that positively-charged, negatively-charged as well as neutral dust particles of 190 nm diameter coexisted for more than one minute after the discharge was switched off. It was also concluded that the transition from ambipolar to free diffusion plays a significant role in determining the residual dust particle charges [15]. In [16], it was shown that diffusion of dust particles in the afterglow can be used to establish several properties of the plasma. Electron and metastable atom densities in an argon/dusty plasma with large dust charge density ($|n_d Z_d| \geq n_e$, where Z_d is the dust charge number in units of elementary charge e, n_e and n_d are the densities of

electrons and dust particles, respectively) were analyzed experimentally and numerically in [17 – 21] for the afterglow and pulsed regimes. In [22], effects of dust particles on the electron energy distribution function in the temporal afterglow were studied analytically. Experimentally, the charge of micro-particles in the spatial afterglow (remote plasma) of an inductively-coupled low pressure RF plasma was measured in [23].

However, in most of the theoretical and numerical studies of the temporal afterglows of dusty plasmas, spatially-averaged (0D) models were used to describe plasma properties. Naturally, the 0D models did not provide information about the spatial distribution of plasma parameters and forces affecting dust grains and about motion of the dust particles.

Plasma inhomogeneity effects and dust motion were taken into account in the models of Schweigert and Alexandrov [24] and Kravchenko *et al* [25], where dusty plasma afterglows were studied using PIC-MCC simulations. In [26], the behavior of a nanodusty plasma afterglow was examined, using a sectional model and also accounting for the plasma inhomogeneity and the transport of dust particles due to the effect of different forces. 1D and 2D models for description of dust grain charging in nonstationary air plasmas, including the decaying streamer-channel plasma, were developed in [27, 28]. However, the results concerning the dynamics of dust particles in afterglow plasmas were not presented in the above-mentioned works [24 – 26, 28]. Knowledge about the dynamics of dust particles and the forces affecting dust grains in afterglow plasmas is important for control of dust particles in plasma technologies, in particular, in those where pulsed plasmas are used [29, 30].

In this paper, we study the dynamics of dust particles in an afterglow plasma. Motion of dust grains in the plasma at different external conditions (dust particle size, neutral gas pressure and initial electron density) is analyzed with or without the gravity force. Electron and ion densities, ion drift velocity and electric field are calculated as functions of spatial coordinate and afterglow time, using the diffusion approach and taking into account the transition from ambipolar to free diffusion. Using these dependencies, electric charges of the dust grains, the forces affecting the grains, as well as the velocities and coordinates of the grains in the plasma afterglow are determined.

2. Theoretical model

2.1. Diffusion model of the plasma

An argon plasma containing singly charged positive ions and electrons, as well as neutral particles is located in a cylindrical discharge chamber of large aspect ratio ($L << D$, where L and D are the height and diameter of the plasma, respectively), so that all plasma parameters depend only on the coordinate x perpendicular to the planes bounding the plasma slab. It is assumed that electrons have Maxwellian distribution and are at temperature T_e considered to be spatially uniform for simplicity. Therefore, the plasma is symmetrical with respect to the center of the slab $x = 0$, and T_e is only dependent of the afterglow time t. In the afterglow, it is assumed that T_e decreases until a certain temperature T_{aft} (~ 0.1 eV) and then stays constant. This temperature can be slightly larger than the gas temperature due to the production of energetic electrons in metastable–metastable collisions and super-elastic electron–metastable collisions. Ions and dust particles are assumed to be at gas temperature T_g (= 0.026 eV). For the glow phase (t = 0), the plasma is assumed to be quasineutral, $n_e = n_i \equiv n$, where n_i is the ion density While in the afterglow (t >0), $n_e \leq n_i$. The electron and ion densities are functions of x and t.

We assume that there is an isolated dust particle of radius a_d in the plasma. We shall study the dust charge and motion of the dust particle in the afterglow plasma. The effect of the dust grain on the electron temperature as well as the electron and ion densities is assumed to be negligible.

The plasma can be described using the diffusion approach [31], assuming that the flux (its x-component) of a species α ($\alpha = i$ or e denotes the ions or electrons) to the walls is [31]

$$\Gamma_\alpha = \pm \mu_\alpha n_\alpha E_s - D_{\alpha f} \partial n_\alpha / \partial x , \qquad (1)$$

where the signs "+" and " – " are for ions and electrons, respectively, $\mu_\alpha = e / m_\alpha \nu_{\alpha n}$ and $D_{\alpha f} = eT_\alpha / m_\alpha \nu_{\alpha n}$ are the mobility and free diffusion coefficients, respectively. Here, m_α and $\nu_{\alpha n}$ are, respectively, the mass and frequency for momentum transfer collisions of species α with neutrals. For argon plasma considered here, $\nu_{in} \approx 2P \times 10^7\ \mathrm{s}^{-1}$ [32], where P is the neutral gas pressure in Torr. The expression for ν_{en} as a function of electron temperature was taken from [33]. E_s is the electric field generated by the difference in the electron and ion densities, i.e., the space-charge field. For t = 0, it is assumed that $E_s = E_a = \frac{D_{if} - D_{ef}}{\mu_i + \mu_e} \frac{\partial n / \partial x}{n}$ and $\Gamma_i = \Gamma_e = -D_a \partial n / \partial x$, where E_a is the ambipolar electric field and $D_a = \frac{\mu_e D_{if} + \mu_i D_{ef}}{\mu_e + \mu_i} \approx D_{if}\left(1 + \frac{T_e}{T_i}\right)$ is the ambipolar diffusion coefficient [31]. At t = 0, we assume that the electron and ion diffusion coefficients D_e and D_i equal to D_a.

For the afterglow phase, $\Gamma_i = -D_i \partial n_i / \partial x$ and one gets from equation (1) that $E_s = \frac{D_{if} - D_i}{\mu_i} \frac{\partial n_i / \partial x}{n_i}$. Taking into account the transition from ambipolar to free diffusion in the afterglow, we assume that D_i is a function of Λ / λ_{De}, where

$\Lambda = L/\pi$ is the diffusion length and λ_{De} is the electron Debye length. Here, it is assumed that $D_i = D_{if} + (1.5D_a - D_{if})[1.0 - \exp\{-\Lambda^2/(4.5\lambda_{De}^2)\}]$ for $\Lambda^2/\lambda_{De}^2 < 150$, $D_i = 1.5 \times D_a / \left\{\frac{1}{2}\left[\frac{\Lambda^2/\lambda_{De}^2 - 150}{3000-150}\right]^{0.4} + 1\right\}$ for $150 \le \Lambda^2/\lambda_{De}^2 < 3000$ and $D_i = D_a$ for $\Lambda^2/\lambda_{De}^2 \ge 3000$. The dependence of D_i on Λ/λ_{De} approximates well the measured dependence in [34] in the case when $T_e = T_i$. In the afterglow, it is assumed that the diffusion coefficient of electrons D_e as a function of Λ/λ_{De} is described by empirical formulas (40) and (41) in [35], which were initially obtained in [36]. In our model, the transition from ambipolar to free diffusion takes place when $\Lambda/\lambda_{De} \le 10$, as in most of the experimental and theoretical works on the transition [34 – 37], excepting [38], where the transition starts at $\Lambda/\lambda_{De} \sim 100$.

The electron and ion densities, as functions of coordinate x and time t, can be found from the continuity equations, respectively

$$\partial n_e/\partial t - D_e \partial^2 n_e/\partial x^2 = \nu^i n_e, \quad (2)$$

$$\partial n_i/\partial t - D_i \partial^2 n_i/\partial x^2 = \nu^i n_e, \quad (3)$$

where $\nu^i = n_a \times 2.39 \times 10^{-8} T_e^{0.57} \exp(-17.43/T_e)$ [39] is the ionization frequency, n_a is the neutral gas atom density in cm^{-3}.

Then, introducing a separation of variables, $n_\alpha(x,t) = n_0 \times \cos(\pi x/L) n_{1\alpha}(t)$, we obtain

$$(1/n_{1e})\partial n_{1e}/\partial t = -D_e \pi^2/L^2 + \nu^i, \quad (4)$$

$$(1/n_{1i})\partial n_{1i}/\partial t = -D_i \pi^2/L^2 + \nu^i n_{1e}/n_{1i}, \quad (5)$$

where $n_0 = n(x=0,t=0)$ and $n_{1\alpha}(t=0) = 1$. Here, it is assumed that the cosine profiles for n_α are kept during the whole afterglow that agrees well with results of previous authors [40, 41].

For $t = 0$ (when $\partial/\partial t = 0$, $n_e = n_i$ and $D_e = D_a$), one obtains from equation (4) the following expression

$$D_a(T_{e0})\left(\frac{\pi}{L}\right)^2 = \nu^i(T_{e0}), \quad (6)$$

which determines the initial electron temperature T_{e0}.

The spatial dependence for the ion density [$n_i \sim \cos(\pi x/L)$] also determines the x-component of the ion drift velocity

$$u = -\frac{D_i}{n_i}\frac{\partial n_i}{\partial x} = D_i \frac{\pi}{L}\tan(\pi x/L). \quad (7)$$

The electron temperature as a function of time in the afterglow can be found from the volume-averaged electron energy balance equation

$$\frac{\partial}{\partial t}\left(\frac{3}{2}e\langle n_e\rangle T_e\right) = -\frac{P_{loss}}{V}, \quad (8)$$

where V is the plasma volume, $P_{loss} = P_{coll} + P_w$ and $\langle n_\alpha \rangle$ is the volume averaged density of species α. For the conditions considered here, $\langle n_\alpha \rangle = \frac{1}{L}\int_{-L/2}^{L/2} n_0 \cos(\pi x/L) n_{1\alpha}(t)dx = \frac{2}{\pi} n_0 n_{1\alpha}(t)$.

$P_{coll} = e\langle n_e\rangle V\left(\sum \nu_j^* U_j^* + \frac{3m_e}{m_a}\nu_{en}(T_e - T_g)\right)$ is the power loss due to elastic and inelastic electron-neutral collisions, ν_j^* and U_j^* are the non-elastic collision frequency and excitation threshold energy for the jth level (including ionization), respectively. The term P_{coll} was calculated using the cross-sections for elastic and inelastic collisions of electrons with argon atoms from [42]. The power loss on the walls is $P_w = e\pi^2 V\left(\langle n_i\rangle D_i \varepsilon_i + \langle n_e\rangle D_e \varepsilon_e\right)/L^2$, where $\varepsilon_{i,(e)}$ is the mean kinetic energy lost per ion (electron) lost [31, 39].

2.2. Dust charge and forces affecting a dust particle

A dust particle in the plasma collects electrons and ions and, as a result, has an electric charge. The dust charge in the glow regime may be found assuming an equal flux of ions and electrons to its surface. This approach also allows to estimate the dust charge in the afterglow plasma [24].

In the pressure range studied (30-150 mTorr), electron-neutral collisions are not important and the orbital motion limited (OML) expression for the electron flux [43] is applicable

$$I_e = \chi n_e \sqrt{m_i/2\pi m_e}\exp(-z), \quad (9)$$

where $\chi = 4\pi a_d^2 \sqrt{eT_e/m_i}$, $z = e|Z_d|/a_d T_e$.

The ion flux to a dust particle is calculated using the interpolation formula proposed by Khrapak *et al* [44]

$$I_i = \chi n_i / (j_{WC}^{-1} + j_{HC}^{-1}), \quad (10)$$

where $j_{WC} = j_i^{OML} + \Delta j_i^{coll}$,

$$j_i^{OML} = \frac{1}{4\xi\sqrt{2\pi\tau}}\left[\sqrt{\pi}(1 + 2\xi^2 + 2z\tau)\mathrm{erf}(\xi) + 2\xi\exp(-\xi^2)\right],$$

$\xi = M\sqrt{\tau/2}$, $M = u/C_s$ is the Mach number, and u is the ion drift velocity determined by equation (6), $C_s = \sqrt{eT_e/m_i}$ is the ion sound speed, and $\tau = T_e/T_i$. The term j_i^{OML}

describes the collisionless (OML) contribution to the ion flux, while the term Δj_i^{coll} accounts for the effect of ion-neutral collisions in the weakly collisional regime [44]:

$$\Delta j_i^{\text{coll}} \approx \frac{\omega_c L_e^3}{3[1+f(\xi)\tau]^{3/2}} \ln^3\left[1+\frac{z\tau\sqrt{1+f(\xi)\tau}}{L_e(1+\xi^2)}\right], \qquad (11)$$

where $\omega_c = \nu a_d / C_s$ is the reduced ion-neutral collision frequency, $f(\xi) = (1+2\xi^2)^{-1}$, and $L_e = \lambda_{De} / a_d$. Here, $\nu = n_a \sigma_{ia} \sqrt{8eT_i/\pi m_i + u^2}$ is the effective ion-neutral collision frequency, $\sigma_{ia} \approx 10^{-14}$ cm^2 is the cross-section for ion-neutral collisions in argon plasma. In the highly collisional regime, the term describing ion-neutral collisions is [44]

$$j_{\text{HC}} = \begin{cases} z/\omega_c, & M \le z/\omega_c, \\ M(1+z/M\omega_c)^2/4, & M > z/\omega_c. \end{cases} \qquad (12)$$

The main forces affecting a charged dust particle in the afterglow are the electric, ion drag, neutral drag and gravity forces. The electric force is

$$\vec{F}_{\text{el}} = eZ_d \vec{E}_s. \qquad (13)$$

For the ion drag force $\vec{F}_{id}$, we use the same approach as in [45, 46], where results from [47–49] were used:

$$\vec{F}_{id} = n_i m_i u_i \vec{u} \times \times \left\{\sigma_c(u_i) + \pi\rho_0(u_i)^2\left[\Lambda(u_i) + \text{K}(\lambda_D(u_i)/\lambda_{in})\right]\right\}, \qquad (14)$$

where $\lambda_D = 1/\sqrt{4\pi n_e e/T_e + 4\pi n_i e^2/m_i u_i^2}$ is the Debye length [50], $u_i = \sqrt{8eT_g/\pi m_i + u^2}$, $\lambda_{in} = 1/n_a\sigma_{ia}$ in the ion mean free path, $\rho_0(u_i) = 2e^2|Z_d|/m_i u_i^2$ is the Coulomb radius, $\sigma_c(u_i) = \pi a_d^2(1+\rho_0(u_i)/a_d)$ is the ion capture cross section, and $\Lambda(u_i) = \ln\left[\frac{\rho_0(\tilde{u}_i)+\lambda_D(\tilde{u}_i)}{\rho_0(\tilde{u}_i)+a_d}\right]$ is the Coulomb logarithm.

In the calculation of the Coulomb logarithm, following to [46, 49], instead of u_i we use the following expression:

$$\tilde{u}_i = \sqrt{8eT_g/(\pi m_i) + u^2\left[1+\left(|u|/(k_\lambda C_s)\right)^3\right]}, \qquad (15)$$

where $k_\lambda = 0.6 + 0.05\ln(m_a) + (\lambda_{De}/5a_d)(\sqrt{T_i/T_e} - 0.1)$, m_a denotes the atomic mass of the ions: $m_a = 40$ for argon. The collisional function K in equation (14) is given by [46, 48]

$$\text{K}(x) = x\arctan(x) + \left(\sqrt{\frac{\pi}{2}} - 1\right)\frac{x^2}{x^2+1} - \sqrt{\frac{\pi}{2}}\ln(1+x^2).$$

The neutral drag force acts in the direction opposite to the motion of dust particle [44, 51, 52],

$$\vec{F}_{nd} = -\frac{4}{3} n_a m_n \vec{V}_d \upsilon_{Tn} \pi a_d^2 \left(1+\frac{\pi}{8}\right), \qquad (16)$$

where m_n is argon atom mass, $\vec{V}_d$ is the velocity of dust particle relative to the stationary background of neutrals (here, gas flows are absent), and $\upsilon_{Tn} = \sqrt{8eT_g/\pi m_n}$ is the average thermal velocity of argon atoms.

In laboratory experiments, dust particles are affected by the force of gravity $\vec{F}_g = m_d \vec{g}$, where $m_d = \rho_d \frac{4}{3}\pi a_d^3$, ρ_d is the dust material density, and $g \approx 980$ cm/s^2 is the gravitational acceleration.

In a gas with a temperature gradient, the particle is also affected by the thermophoretic force [53]. However, we assume that the gas temperature gradients are small and neglect this force.

The particle motion in the afterglow is given by

$$\frac{d\vec{V}_d}{dt} = \vec{g} + \frac{\vec{F}_{el} + \vec{F}_{id} + \vec{F}_{nd}}{m_d}, \qquad (17)$$

which determines the *x*-component of the particle velocity (other components are assumed to be zero because of the geometry of the problem). Knowing V_d, one can find the particle coordinate x_d:

$$V_d = \frac{dx_d}{dt}. \qquad (18)$$

The kinetics of dust particle discharging is described by the equation

$$\frac{d|Z_d|}{dt} = I_e - I_i. \qquad (19)$$

Equations (17) – (19) should be accompanied by initial conditions. At $t = 0$, we assume that the dust particle is immobile ($V_d(t=0) = 0$) and its initial coordinate x_0 is found assuming that the forces affecting the dust grain balance each other [$m_d\vec{g} + \vec{F}_{el}(t=0) + \vec{F}_{id}(t=0) = 0$]. The dust charge at $t = 0$ is found assuming that the ion flux to a dust particle equals to that of electrons. Equations (4), (5), (8), (17) – (19) are solved numerically by using the DVODE package [54].

3. Results

Calculations have been carried out for different dust radii, neutral gas pressures, initial electron densities and with or without gravity.

3.1. Dust radius variation

First, assuming that $\vec{F}_g = 0$, we have studied how dust charge and motion depend on dust size. In figure 1(*a*), the dust

charge as a function of time is presented for different dust radii. The unnumbered curves in figure 1(*a*) describe the charge obtained from equation (19), while the curves 1, 2, 3 and 4 are for the dust charge $Z_d = Z_{d1}$, where Z_{d1} is the root of equation $I_e = I_i$. The time-dependencies for dust charge are calculated for P = 30 mTorr , n_0= 10^{10} cm^{-3}, L = 5 cm, T_{aft} =0.1 eV and assuming that the dust particle is in equilibrium in the plasma slab at t = 0.

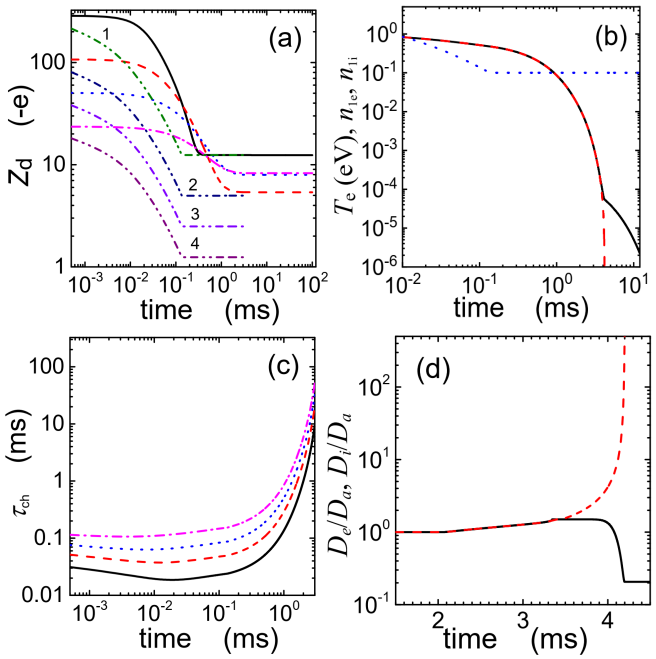

Figure 1. The dust charge (*a*); $n_i(x=0)/n_0$ (solid line), $n_e(x=0)/n_0$ (dashed line) and T_e (dotted line) (*b*); the dust charging time (c) and D_e/D_a (dashed line) and D_i/D_a (solid line) (*d*) as functions of time. In figure 1(*a*), the unnumbered solid, dashed, dotted and dash-dotted curves for Z_d are obtained from equation (19) and curves 1, 2, 3 and 4 are calculated from $I_e = I_i$, line styles corresponding to a_d = 50 nm, 20 nm, 10 nm and 5 nm, respectively (same styles in figure 1(*c*)). Here, P= 30 mTorr and n_0= 10^{10} cm^{-3}.

The initial negative charge increases if a_d becomes larger (figure 1(*a*)) because of a larger surface collecting electrons and ions from the plasma. In the beginning of the afterglow, $|Z_d|$ decreases due to an ion flux larger than the electron one. At $t \le 0.1$ ms, the ion flux dominates over the electron flux mainly due to the rapid decrease of the electron temperature (figure 1(*b*)). The negative charge on the dust particle decreases faster for larger dust sizes due to the larger ion flux ($I_i \sim a_d^2$) leading to possible larger $|Z_d|$ for smaller nanoparticle in the late afterglow (figure 1 (*a*)). This is due to an increasing charging time as particle size decreases (figure 1(*c*)). As a result, the charge of small nanoparticles varies slowly in the afterglow and becomes "frozen" when the electron and ion densities and fluxes are very small and with $I_i > I_e$ [at $t \ge 2.5$ ms for $a_d < 10$ nm in figure 1(*a*)]. This is opposite to the case of large nanoparticles (for example, for a_d = 50 nm) when the charge becomes frozen before the vanishing of electrons and ions from the plasma (figures 1(*a*) and 1(*b*)). In this case, the charging time is small in the beginning of afterglow (figure 1(*c*)), and, therefore, $|Z_d|$ drops rapidly and the dust charge becomes frozen when $I_e \approx I_i$ (figure 1(*a*)).

The time-dependencies for charging time in figure 1(*c*) are obtained from the expression [11]

$\tau_{ch} = 1.0/(I_e^{/} - I_i^{/})\big|_{Z_d = Z_{d1}}$, where $I_e^{/} = \partial I_e / \partial Z_d$ and $I_i^{/} = \partial I_i / \partial Z_d$. In the OML approximation [11],

$$\tau_{ch} = \left[I_e \frac{e}{a_d T_e} \frac{1+\tau+\tau z}{1+\tau z} \right]^{-1} \Bigg|_{Z_d = Z_{d1}} . \qquad (20)$$

Since $I_e \propto n_e a_d^2 \sqrt{T_e} \exp(-z)$ and the decrease of T_e in the very beginning of afterglow is faster than the decrease of $|Z_d|$ and n_e, τ_{ch} decreases with time for $t \le 10^{-2}$ ms (figure 1(*c*)). At $t > 0.1$ ms (when $T_e = T_{aft}$), the charging time increases because of decreasing n_e. From equation (20) it follows that $\tau_{ch} \propto 1/a_d$, according to the dependencies in figure 1(*c*).

Note that the transition from ambipolar to free diffusion does not affect much on the dust charge dependences for the conditions here, because it is observed at rather large afterglow times (at $t \ge 3.5$ ms in figure 1(*d*)) when I_e and I_i are small due to small n_e and n_i (figure 1(*b*). For example, $Z_d(t$ = 1ms) = - 12.42 and $Z_d(t$ = 10 ms) = - 12.39 for the 50 nm case.

Note that equation (19) does not give the real value of dust charge in the afterglow, especially for small dust size due to charge discreteness. It provides an approximate value for the dust charge, and the real one fluctuates around this value [55]. If there are many dust particles of the same size in the plasma, a more accurate description of dust charging can be made by calculating the dust charge distribution [56]. In most stationary cases, this distribution is close to the Gaussian distribution with the variance σ^2 described by the following expression [56]

$$\sigma^2 = \frac{(I_e + I_i)/2}{I_e^{/} + I_e^{//}/2 - I_i^{/} + I_i^{//}/2} \Bigg|_{Z_d = Z_{d1}} , \qquad (21)$$

where $I_\alpha^{//} = \partial I_\alpha^{/} / \partial Z_d$.

In the OML approximation and when $I_\alpha^{/} >> I_\alpha^{//}$, equation (21) gives

$$\sigma^2 = \frac{a_d T_e}{e\left[1 + \tau/(1+\tau z)\right]} \Bigg|_{Z_d = Z_{d1}} . \qquad (22)$$

In figure 2(*a*), σ, which characterizes the width of the dust charge distribution obtained from equation (21), is shown for different dust radii. At $t \le 0.1$ ms, the width of the dust charge distribution is larger for larger a_d (figure 2(*a*)),

according to equation (22) showing that $\sigma^2 \propto a_d$. For large afterglow times (t > 1 ms), σ is smaller for a_d=20 nm than for 50 nm, while for a_d =5 nm and 10 nm σ is nearly the same and larger than at 50 nm (figure 2(*a*)). In our opinion, this is due to larger values of $z = e|Z_d|/a_d T_e$ at late afterglow times in the cases of a_d =5 nm and 10 nm compared to 50 nm and 20 nm cases.

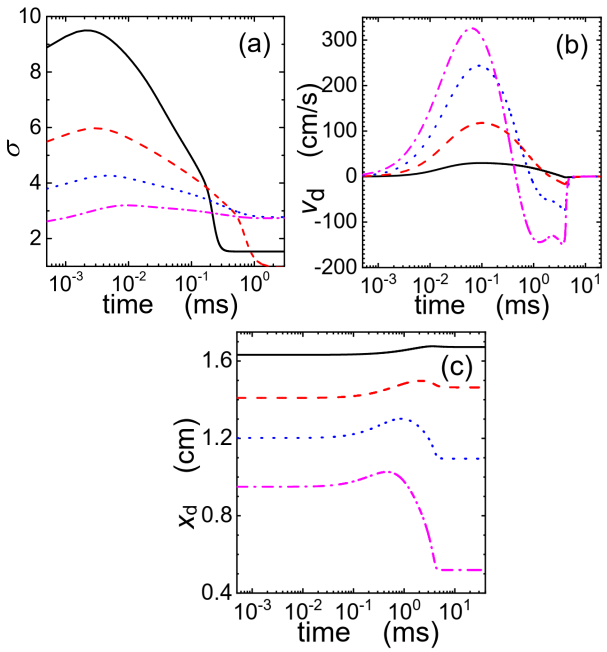

Figure 2. σ (*a*), the dust velocity (*b*) and coordinate (*c*) as functions of time for different dust radii: 50 nm (solid line), 20 nm (dashed line), 10 nm (dotted line) and 5 nm (dash-dotted line). The other conditions are the same as in figure 1.

Figure 2(*b*) shows that the dust velocity grows in the beginning of afterglow until a maximum value, v_{max}, at a time t_1 (figure 2(*b*)). The dust acceleration at $t < t_1$ is positive ($dV_d/dt > 0$) (figure 2(*b*)) because the ion drag force is larger than the electric force. Indeed, the electric force decreases faster because of the rapid decrease of T_e (figure 1(*b*)). At $t = t_1$, the geometric sum of ion drag, electric and neutral drag forces is zero, and the dust acceleration vanishes (figure 2(*b*)).

The dust velocity grows faster in the very beginning of afterglow ($t < t_1$) if the dust radius becomes smaller (figure 2(*b*)). Whereas the forces affecting the dust grain decrease with decreasing a_d (figure 3), the nanoparticle mass (with a_d^3 dependency) decreases faster than the forces resulting in faster motion for a smaller nanoparticle. Since the Coulomb part of the ion drag force, described by the second term in the braces of equation (14), is proportional to Z_d^2 and $F_{el} \sim Z_d$, with decreasing a_d, the ion drag force in the central part of the plasma slab decreases faster than the electric force (figure 3). As a result, the initial location of the nanoparticle becomes closer to the slab midplane when the dust radius decreases. Because a decrease of a_d is accompanied by increasing V_d, the variation of nanoparticle coordinate in the afterglow may be essential for nanoparticles of small radius (figure 2(*c*)). In particular, a nanoparticle with a radius of 5 nm can change its coordinate during the afterglow by 0.5 cm (figure 2(*c*)).

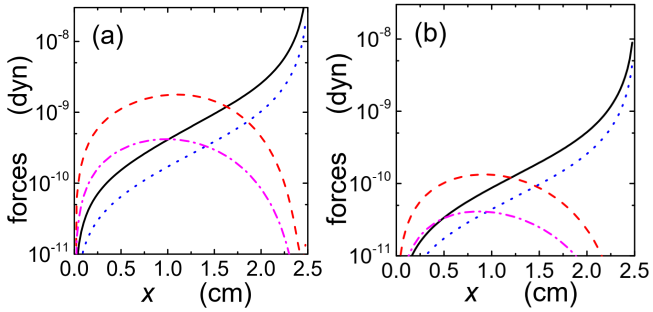

Figure 3. The initial spatial distributions of $|\vec{F}_{el}|$ and $|\vec{F}_{id}|$ for a_d= 50 nm and 20 nm (*a*) and a_d= 10 nm and 5 nm (*b*). In figure 3(*a*) [figure 3(*b*)], the solid and dotted curves correspond to $|\vec{F}_{el}|$, while the dashed and dash-dotted curves $-|\vec{F}_{id}|$ for a_d = 50 nm and 20 nm [a_d = 10 nm and 5 nm], respectively. The other conditions are the same as in figure 1.

For t > 0.1 ms, the ion drag force decreases faster than the electric force because T_e is time-independent (figure 1(*b*)). For large afterglow times ($t \geq 2$ ms), Z_d is nearly time-independent (figure 1(*a*)) and F_{el} evolves mainly because of the variation of the ion diffusion coefficient ($E_s \propto D_{if} - D_i$), while $|F_{id}|$ becomes smaller due to the ion density decrease. In the time interval $t_1 < t < t_2$, where t_2 corresponds to the time when V_d changes sign, $|F_{el}| + |F_{nd}| > |F_{id}|$. For the time interval $t_2 < t < t_3$, where t_3 corresponds to the time when V_d is minimal (for the case of a_d =5 nm, t_3 corresponds to the first minimum of V_d), $|F_{el}| > |F_{nd}| + |F_{id}|$. The dust particle moves to the slab boundary at $t < t_2$ and in the opposite direction at $t_2 < t < t_3$. There is the minimum at $t = t_3$ in the time-dependence for dust velocity (figure 2(*b*)), which is observed at rather large afterglow times ($t \geq 1$ ms), when $|F_{el}| >> |F_{id}|$, $|F_{el}| \approx |F_{nd}|$ and, therefore, for the minimum, $V_d \approx |eZ_d E_s| / \left[\frac{4}{3} n_a m_n \upsilon_{Tn} \pi a_d^2 \left(1 + \frac{\pi}{8}\right)\right]$. For smaller nanoparticles, this minimum can be observed at smaller times (as for the 5 nm case in figure 2(*b*)) because they move faster. Moreover, for small nanoparticles (here, for a_d =5 nm), the time-dependence for V_d may have two minimums. The second minimum (at $t = t_4$) is due to increasing the electric field in the time interval 2 ms $\leq t \leq 3.5$ ms (because of increasing D_i (figure 1(*d*)). In our opinion, we do not observe for the second minimum in the $V_d(t)$ dependence for large nanoparticles ($a_d \geq 10$ nm), because of larger times required to accelerate

these particles to the velocities corresponding to the minimum at $t = t_3$, as compared with the a_d =5 nm case. At $t \geq 4$ ms, the ion diffusion coefficient decreases (figure 1(*d*)), and, therefore, E_s and F_{el} become smaller and $|V_d|$ decreases rapidly with time because of the effect of neutral drag force. The electric field vanishes when $D_i = D_{if}$. At $t > t_3$ for $a_d \geq 10$ nm and at $t > t_4$ for $a_d = 5$ nm, $|V_d|$ also decreases with time due to dust motion towards the slab center (figure 2(*c*)) where the electric force affecting the dust grain is smaller (figure 3).

We also considered the case when a dust particle is additionally affected by the gravity force. Figures 4(*a*) and 4(*b*) show V_d and x_d calculated for the case when the initial location of the dust grain is near the bottom slab boundary, while it's near the top boundary in figures 4(*c*) and 4(*d*). These two equilibrium positions are usually observed in experiments such as in [5, 12 – 14].

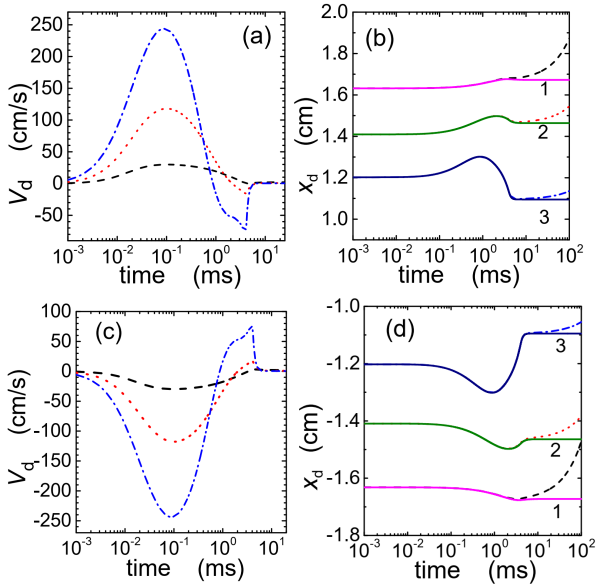

Figure 4. The dust velocity [(*a*) and (*c*)] and coordinate [(*b*) and (*d*)] for different dust radii. The dashed, dotted and dash-dotted curves correspond, respectively, to a_d=50 nm, 20 nm and 10 nm in the case when $\vec{F}_g \neq 0$. The curves 1, 2 and 3 in figures 4(*b*) and 4(*d*) are, respectively, for a_d=50 nm, 20 nm and 10 nm in the case when $\vec{F}_g = 0$. Figures 4(*a*) and 4(*b*) correspond to the case when the dust particle is initially located near the bottom slab boundary, while figures 4(*c*) and 4(*d*) – near the top boundary. The *x*-axis and $m_d\vec{g}$ are directed to the bottom slab boundary, and x = 0 corresponds to the midplane of the plasma slab. Here, $\rho_d = 1.5\,\mathrm{g/cm^3}$ and the other conditions are the same as in figure 1.

It follows from figure 4 that the gravity force does not affect essentially nanoparticle motion at small afterglow times (t < 10 ms). However, for large afterglow times ($t \geq$10 ms), when the both ion drag force and electric force vanish, the dust motion is due to the gravity and neutral drag forces. At large afterglow times, a dust grain moves to the slab boundary with a constant velocity $\left(V_d = F_g \Big/ \left[\frac{4}{3} n_a m_n \upsilon_{Tn} \pi a_d^2 \left(1 + \frac{\pi}{8}\right)\right]\right)$, which is proportional to a_d. At t > 15 ms, the dust velocity for a_d = 10 nm, 20 nm and 50 nm is 0.41 cm/s, 0.82 cm/s and 2.05 cm/s, respectively. The absolute value of the dust velocity at late afterglow times is the same in figure 4(*a*) and figure 4(*c*). Thus, at late afterglow times, due to the effect of the gravity and neutral drag forces, a dust particle moves with a constant velocity to the bottom electrode. The velocity increases with increasing dust size. Eventually, the dust particle may deposit on the bottom electrode or take a new equilibrium position if an additional force (for example, the thermal force [13 – 15]) affects the particle after the plasma is off.

3.2. Pressure effect

Next consider how plasma parameters and dust charge and motion depend on neutral gas pressure. Since we have shown in previous subsection that the ion drag and electric forces may affect essentially particle motion in the plasma afterglow if the size of dust particle is small, our study of gas pressure effects is focused on small nanoparticles (here, a_d = 10 nm). In this study, it is assumed that $\vec{F}_g = 0$.

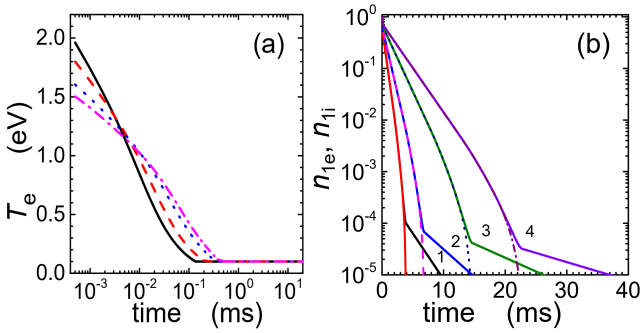

Figure 5. The electron temperature (*a*) and the normalized electron and ion densities at x = 0 (*b*) as functions of time for different neutral gas pressures. The unnumbered solid, dashed, dotted and dash-dotted curves for T_e and n_e and the curves 1, 2, 3 and 4 for n_i correspond to 30 mTorr, 50 mTorr, 100 mTorr and 150 mTorr, respectively. Here, P_{in} =10^{-2} W/cm^2. n_0 is 5.39×10^9 cm^{-3}, 8.67×10^9 cm^{-3}, 1.51×10^{10} cm^{-3} and 2.02×10^{10} cm^{-3} for 30 mTorr, 50 mTorr, 100 mTorr and 150 mTorr, correspondingly. The other conditions are the same as in figure 1.

Figures 5(*a*) and 5(*b*) show, correspondingly, the time-dependencies for T_e and for the normalized electron and ion densities ($n_\alpha(x=0)/n_0$) obtained for different P. These dependencies are calculated for a fixed input power per unit area at t = 0 P_{in}, which in our case is $[P_{coll}(t=0) + P_w(t=0)]L/V$.

For the conditions corresponding to figure 5, T_e at t = 0 is 2.53 eV, 2.19 eV, 1.85 eV and 1.69 eV for 30 mTorr, 50 mTorr, 100 mTorr and 150 mTorr, respectively. The initial electron temperature decreases with increasing pressure, that agrees well with measurements in [57]. Moreover, the electron temperature and the electron and ion densities decrease faster if P is smaller. This conclusion agrees well with results of previous authors (figure 5 in [58], figure 9 in [59]). The faster decrease is mainly due to increasing the ion and electron diffusion coefficients. With increasing pressure, the initial electron density in the case of fixed input power becomes larger, that agrees well with results of previous authors (figure 6 in [60]).

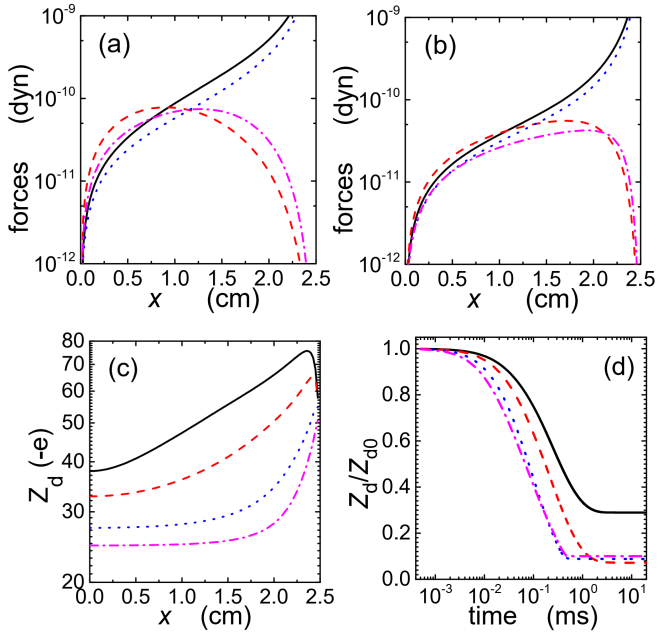

Figure 6. The initial spatial distributions of $\left|\vec{F}_{el}\right|$ and $\left|\vec{F}_{id}\right|$ for P = 30 mTorr and 50 mTorr (*a*) and P= 100 mTorr and 150 mTorr (*b*). In figure 6(*a*) [figure 6(*b*)], solid and dotted curves correspond to $\left|\vec{F}_{el}\right|$, while the dashed and dash-dotted curves $-\left|\vec{F}_{id}\right|$ for P = 30 and 50 mTorr [P = 100 and 150 mTorr], respectively. (*c*) The dust charge at t = 0 as a function of x-coordinate and (*d*) the normalized dust charge as a function of time for different P: 30 mTorr (solid line), 50 mTorr (dashed line), 100 mTorr (dotted line) and 150 mTorr (dash-dotted line). $|Z_{d0}|$ is 46.22, 37.42, 28.08 and 24.74 for P =30 mTorr, 50 mTorr, 100 mTorr and 150 mTorr, respectively. a_d = 10 nm, x = 0 corresponds to the midplane of the plasma slab and the other conditions are the same as for figure 5.

It is found that the initial equilibrium location of the grain x_0 depends strongly on gas pressure. With increasing pressure, the coordinate grows at P<70 mTorr and decreases at larger pressures. In particular, x_0 = 0.93 cm, 1.16 cm, 1.22 cm,1.08 cm and 0.44 cm for 30 mTorr, 50 mTorr, 70 mTorr, 100 mTorr and 150 mTorr, respectively. The effect of gas pressure on the x_0 location is due to differences in the spatial distributions of $|F_{el}|$ and $|F_{id}|$ at different P, as shown in figures 6(*a*) and 6(*b*).

With increasing pressure, the initial electric force decreases in the whole plasma volume (figures 6(*a*) and 6(*b*)) due to decreasing the electron temperature ($E_a \approx -T_e \frac{\partial n / \partial x}{n}$ for t =0) and the dust charge (figure 6(*c*)). Because of decreasing T_e and $|Z_d|$, the ion drag force in central part of the plasma slab (at $|x| \le 1.0$ cm) also becomes smaller when P is larger. Moreover, the shape of initial spatial distribution of $|F_{id}|$ also depends on neutral gas pressure. With increasing P, the maximum of $|F_{id}|$ becomes closer to the slab boundary (figures 6(*a*) and 6(*b*)). In our opinion, the variation of spatial distribution of $|F_{id}|$ is due to the dependence of spatial distribution for dust charge on pressure (figure 6(*c*)). With increasing x, $|Z_d|$ at t = 0 increases in the whole plasma volume at large pressures, while the dust charge may decrease near the slab boundary at small pressures (for example, at P = 30 mTorr) (figure 6(*c*)). In our opinion, this is due to higher ion drift velocity at smaller pressure. Due to decreasing the ion drift velocity with an increase of P, the spatial distribution of dust charge becomes more spatially homogeneous in the central part of discharge (at x < 1.5 cm) (figure 6(*c*)). Moreover, because of enhancement of ion-neutral collisions in the sheath around the dust particle, the amount of negative charge on the dust particle at t = 0 decreases with increasing P (see caption to figure 6 and [61]).

The time-dependence for dust charge is also a function of gas pressure (figure 6(*d*)). As mentioned in the previous subsection, the amount of negative charge on dust particle decreases in the beginning of afterglow due to a higher ion flux to the dust particle comparing with that of electrons. The difference between the ion and electron fluxes depends on the time-dependencies for n_e, n_i and T_e in the afterglow plasma, as well as on the initial dust charge. Since with decreasing pressure, the initial electron density becomes smaller, the absolute value of the ion flux normalized on $|Z_{d0}|$, where $Z_{d0}=Z_d$ (t =0), becomes also smaller, and the normalized dust charge Z_d/Z_{d0} decreases more slowly with time at smaller pressures (here, for $P \le 100$ mTorr) (figure 6(*d*). Note that the difference in the time-dependencies for Z_d/Z_{d0} in the P = 100 mTorr and 150 mTorr cases is small here. In our opinion, this is because of the small difference in the time-dependencies for electron temperature (figure 5). Moreover, since the electron temperature and the electron and ion densities drop faster with a decrease of P (figure 5), the absolute value of "frozen charge" of a dust particle may increase with decreasing pressure (figure 6(*d*)). For the conditions corresponding to figure 6(*d*), $|Z_d|$ at t =2 ms is 13.61, 6.26, 2.99, 2.482 and 2.481 for P =30 mTorr, 40 mTorr, 50 mTorr, 100 mTorr and 150 mTorr, respectively. Note that the value of "frozen charge" depends slightly on P for large pressures ($P \ge$50 mTorr) and

moderate electron densities ($n_0 \sim 10^{10}$ cm^{-3}). This is due to the fast decrease of $|Z_d|$ in the beginning of afterglow and due to the fact that the effect of ion-neutral collisions on the dust charge in the plasma afterglow decreases with increasing t. To check the last conclusion, we analyze the ion current to the dust grain in the case when the ion drift velocity is small, what is typical for most plasma volume at late afterglow times (when $T_e \approx T_{aft}$). For small drift velocities, $I_i \approx n_i a_d^2 \left(8\pi e T_i/m_i\right)^{1/2} \left(1+z\tau+Hz^2\tau^2\lambda_s n_a \sigma_{ia}\right)$ [61], where λ_s is the screening length, which is of the same order as the Debye length [62]. The function H satisfies $H \sim 0.1$ for $0.1 \leq \beta \leq 10$, $H \sim \beta$ for $\beta << 1$ and $H \sim \beta^{-2}(\ln\beta)^3$ for $\beta >> 1$ [61], where $\beta = |Z_d| e/\lambda_s T_i$. With increasing the afterglow time, the ratio of the third term to the second term in the brackets of the expression for I_i becomes smaller because of decreasing τz. As a result, at $t > 2$ ms, ion-neutral collisions for $P \geq 50$ mTorr do not affect essentially the ion current to a dust grain and, consequently, the dependence of dust charge on pressure is essentially smaller at late afterglow times than that at $t = 0$ (the values of Z_{d0} at different pressures are presented in caption to figure 6).

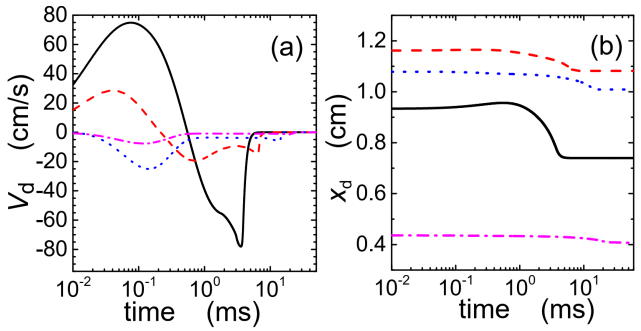

Figure 7. The dust velocity (*a*) and the dust coordinate (*b*) as functions of time for different gas pressures: 30 mTorr (solid line), 50 mTorr (dashed line), 100 mTorr (dotted line) and 150 mTorr (dash-dotted line). The other conditions are the same as for figure 6.

At small pressures and small afterglow times ($t < t_1$), the dust acceleration is positive and the velocity grows with time (figure 7(*a*)). The maximum velocity v_{max} is larger and observed for larger times when P is smaller (figure 7(*a*)). For the case of 100 mTorr, v_{max} is very small and reached very quickly (0.328 cm/s at $t \approx 4.5$ μs), and at 150 mTorr no positive acceleration in the beginning of the plasma afterglow is observed. v_{max} decreases with increasing pressures and a positive acceleration of the dust particle in the beginning of the afterglow is absent at large pressures because of decreasing of $|F_{id}|$ (figure 6). Since with decreasing pressure, the dust velocity becomes maximal at larger times, the time t_3, when V_d is minimal, also increases. Moreover, $|V_d|$ at $t = t_3$ is larger for smaller pressures. This is due to the fact that $|F_{el}| \approx |F_{nd}|$ for $t = t_3$, and the electric force decreases with increasing P (figure 6). As a result, $|V_d(t=t_3)| \propto |F_{el}|/n_a$, i.e., the absolute value of V_d increases when P becomes smaller.

Due to larger values of $|V_d|$, the variation of coordinate of the dust particle in the afterglow plasma is larger for smaller pressures (figure 7(*b*)). The decreasing of the maximum value of $|V_d|$ and of x_d variation with increasing pressure can be also explained by an enhancement of friction due to the effect of neutral drag force.

3.3. Effect of electron density variation

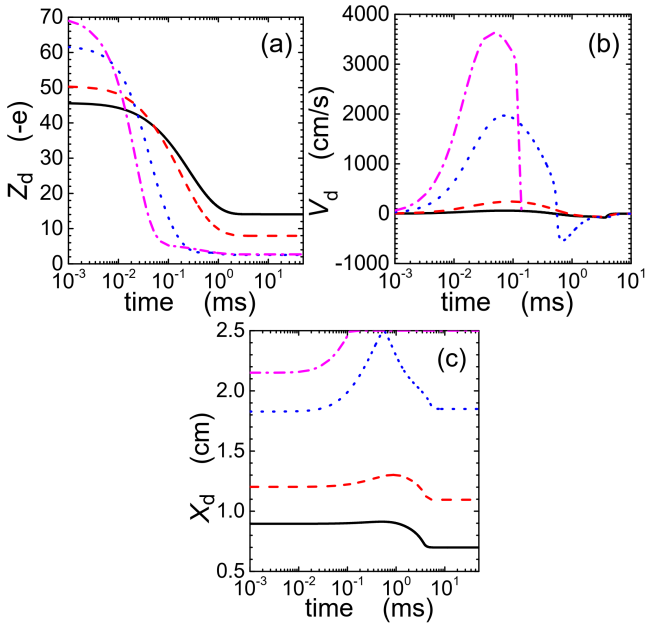

Figure 8. The nanoparticle charge (*a*), velocity (*b*) and coordinate (*c*) as functions of time for a_d = 10 nm, P = 30 mTorr and different initial electron densities in the slab center: $n_0 = 5\times10^9$ cm^{-3} (solid line), 10^{10} cm^{-3} (dashed line), 10^{11} cm^{-3} (dotted line) and 10^{12} cm^{-3} (dash-dotted line). The other conditions are the same as for figure 1.

Assuming that $\vec{F}_g = 0$, we also analyze how the nanoparticle coordinate, velocity and charge depend on the initial plasma density. The initial amount of negative charge on a dust particle increases with increasing n_0 (figure 8(*a*)). In our opinion, this increase is due to decreasing Δj_i^{coll} (equation(11)), because the electron Debye length becomes smaller. $|Z_d|$ decreases faster in the afterglow if n_0 is larger (figure 8(*a*)) because of higher ion flux to the dust grain in the afterglow ($I_i \sim n_0$). Since the absolute value of Z_d increases, the ion drag and electric forces also become larger with an increase of n_0 at small afterglow times. However, the increase of $|\vec{F}_{id}|$ with an increase of n_0 is more essential than that of

$\left|\vec{F}_{el}\right|$ because the Coulomb part of $\left|\vec{F}_{id}\right|$ is proportional to Z_d^2, while $\left|\vec{F}_{el}\right|$ depends linearly on $|Z_d|$. As a result, the initial location of the nanoparticle is closer to the slab boundary if n_0 is larger (figure 8(*c*)). In the very beginning of the afterglow, due to an enhancement of $\left|\vec{F}_{id}\right|$, the nanoparticle moves faster to the slab boundary if n_0 is larger (figure 8(*b*)). Moreover, if the initial electron density is very large ($n_0 \geq 10^{12}$ cm^{-3}), small nanoparticles may quickly reach the plasma boundary (figure 8(*c*)).

4. Conclusion

Thus, behavior of a dust grain in an afterglow plasma has been studied using a 1D model. In contrast to previous works where the dust charge variation in afterglow plasmas was studied using different diffusion models [15, 17, 28], our study also analyzes the dynamics of the dust grain. The analysis has been carried out for different dust radii, gas pressures and initial electron densities.

It has been found that the charge of smaller nanoparticles varies more slowly (figure 1(*a*)) in the afterglow plasma because of smaller ion flux to their surface. Moreover, the absolute value of the negative charge of a small nanoparticle (a_d < 20 nm) in the late afterglow may be larger than the one of a larger nanoparticle (figure 1(*a*)), because of smaller charging time (figure 1(*c*)).

At small pressures ($P \leq$ 50 mTorr), the dust velocity increases in the beginning of plasma afterglow (figure 7(*a*)) because the ion drag force affecting the dust particle is larger than the electric force. The electric force decreases rapidly in the beginning of the afterglow, because of decreasing T_e. In the afterglow, when the electron temperature does not change with time, the ion drag force decreases faster with time than the electric force because of decreasing n_i. Most of time in the afterglow, when the electric field is important, the dust velocity is negative (directed to the slab center) and the dust particle moves to the center (figure 2).

The dust particle dynamics during the afterglow has been examined in microgravity conditions and in presence of gravity. Without gravity, the variation of location of large dust particles ($a_d \geq$ 20 nm) during the afterglow is very small because of a rapid decrease of the ion drag and electric forces. Meantime, smaller nanoparticles are more mobile and the variation of their location in the afterglow may be essential (figure 2(*c*)). In presence of gravity, this force does not affect essentially nanoparticles at small afterglow times (t < 10 ms) (figure 4). At large afterglow times ($t \geq$ 10 ms), when both ion drag force and electric force vanish, the dust motion is governed by the gravity and neutral drag forces. Moreover, the gravity force is balanced by the neutral drag force, and a dust particle moves to the slab boundary with a constant velocity. As it can be expected, gravity plays more essential role for dust particle of larger size. The velocity is larger if the dust radius is bigger. The present study reveals the dynamics and trajectory followed by the dust particle during the fast plasma relaxation. In microgravity, it corresponds to the motion between its equilibrium position in the plasma and its new equilibrium position after the plasma is off.

Dust dynamics depends essentially on gas pressure and the initial electron density. The dust velocities in an afterglow plasma are larger at smaller pressures (figure 7(*a*)). This is due to decreasing the neutral drag force and increasing the initial dust charge and the ion drag and electric forces because of decreasing the ion-neutral collision frequency. Moreover, with decreasing gas pressure at a fixed input power, the dust charge varies more slowly with time in the afterglow plasma because of decreasing the ion flux to the dust particle because the ion density becomes smaller. As a result, at late afterglow times, the amount of negative charge on small dust particles may increase with decreasing pressure (figure 6(*d*)). With increasing the electron density, both $|Z_d|$ and $|V_d|$ increase in the very beginning of the afterglow (figures 8(*a*) and 8(*b*)) because of a decrease of the electron Debye length and an increase of the ion drag force. Due to the increase of the ion drag force, smaller nanoparticles move more rapidly (figure 8(*b*)) and even may leave the plasma volume (figure 8(*c*)). The dust charge decreases faster in the beginning of afterglow if the initial electron density is larger because of larger ion flux to the dust surface.

Note that the results here have been obtained using some simplifications. In particular, we have considered an isolated grain in the plasma slab, while in some experiments [17 – 21], the dust charge density may be large ($|n_d Z_d| \geq n_e$). We also did not account for the charge fluctuations [55, 56, 63, 64], which may affect essentially the dust particle charge (figure 2(*a*)) and trajectories [65] and we considered a mean charge. Moreover, the discharging of dust particles is very sensitive to external conditions in the afterglow, in particular, to external electric fields not considered here [66, 67]. The model also does not consider processes in plasma sheaths.

Our model also assumes that the electron energy distribution is Maxwellian. The Maxwellian approximation usually allows to describe qualitatively plasma properties [31]. The Maxwellian electron energy distribution function (EEDF) is typical for plasmas, where the frequency of the electric field sustaining the plasma is larger than the frequency for electron-atom collisions [68] and when the electron density is large, for example, in microwave discharge plasmas [69]. At certain conditions, the EEDF can also be nearly Maxwellian in inductively-coupled plasmas [57]. Moreover, in RF capacitively coupled plasmas, where the EEDF is usually non-Maxwellian, it may become nearly Maxwellian in the afterglow phase [70] justifying our approximation.

In our model, we also did not consider metastable argon atoms, which may affect essentially the afterglow plasma. In [71], it was shown that in a steady-state plasma, the excited argon atoms influence the power budget mainly due to the power loss in stepwise excitation which dominates for pressures below about 50 Pa. Gorchakov *et al* [71] also found that during the afterglow chemoionization processes and deexciting electron collisions primarily provide power gain of the electron ensemble at pressures below about 10 Pa and the contribution of the excited atoms to the total power loss generally remains smaller than about 15%. Experiments and their analysis carried out in [72] showed that super-elastic collisions between electrons and the long-lived rare gas metastable atoms may affect essentially the electron temperature in the afterglow. In [70], it was obtained that the rates of the electron heating and cooling by reactions with argon metastables, namely, the excitation to the higher energy levels and super-elastic collisions, are almost fully compensated by each other, and the chemionization doesn't have a valuable impact on the electron temperature in the early afterglow of a RF capacitively-coupled argon plasma. Moreover, collisions of metastable atoms with dust particles may affect the dust charge and other properties of afterglow plasmas if the dust charge density is large [17].

In the present work, we consider pressures smaller than 50 Pa and the case of small dust densities. Therefore, we expect that metastable atoms do not affect much on gas discharge properties in the glow phase and in the beginning of afterglow. At late afterglow times, we assume that the electron temperature is 0.1 eV, in particularly, due to collisions of metastable atoms with other species, that agrees with our previous studies on afterglow and pulsed argon plasmas [17, 21]. Note that PIC MC simulations in [70] also showed that the electron temperature at t=0.4 ms in an argon afterglow plasma is essentially larger than the gas temperature (see figure 8 in [70]).

Therefore, the results presented here can be used only for qualitative analysis of dust motion, dust charge and forces affecting the grain in a plasma afterglow. They provide first insights on dust dynamics during the very short time scale of the plasma decay. The model and results here can be a base for building of more complicate models for description of nanoparticle dynamics in an afterglow plasma which will take into account the dust charge fluctuations, effects of metastable argon atoms, processes in plasma sheaths and other effects including possible deviation of the electron energy distribution function from the Maxwellian distribution [22].

The presented results obtained using 1D model on dusty plasma afterglow, are relevant to many applications involving nonstationary plasmas containing impurities, especially plasmas used for the synthesis of novel nanomaterials. The time and spatial dependencies presented here can be useful for benchmarking or verifying experiments and numerical simulations.

References

[1] Vladimirov S V and Ostrikov K 2004 *Phys. Rep.* **393** 175
[2] Fortov V E, Ivlev A V, Khrapak S A, Khrapak A G and Morfill G E 2005 *Phys. Rep*. **421** 1
[3] Bonitz M, Henning C and Block D 2010 *Rep. Prog. Phys.* **73** 066501
[4] Stenflo L, Shukla P K and Yu M Y 2000 *Phys. Plasmas* **7** 2731
[5] Mikikian M and Boufendi L 2004 *Phys. Plasmas* **11** 3733
[6] Boufendi L *et al* 2011 *J. Phys. D: Appl. Phys.* **44** 174035
[7] Levchenko I, Keidar M, Cvelbar U, Mariotti D, Mai-Prochnow A, Fang J and Ostrikov K 2016 *J. Phys. D: Appl. Phys*. **49** 273001
[8] Kersten H, Deutsch H, Stoffels E, Stoffels W W, Kroesen G M W and Hippler R 2001 *Contrib. Plasma Phys.* **41** 598
[9] Ostrikov K, Cvelbar U and Murphy B 2011 *J. Phys. D: Appl. Phys.* **44** 174001
[10] Shukla P K and Mamun A A 2002 *Introduction to Dusty Plasma Physics* (Bristol: Institute of Physics)
[11] Fortov V E, Khrapak A G, Khrapak S A, Molotkov V I and Petrov O F 2004 *Phys.—Usp.* **47** 447
[12] Ivlev A *et al* 2003 *Phys. Rev. Lett.* **90** 055003
[13] Couëdel L, Mikikian M, Boufendi L and Samarian A A 2006 *Phys. Rev.* E **74** 026403
[14] Couëdel L, Samarian A A, Mikikian M and Boufendi L 2008 *IEEE Trans. Plasma Sci*. **36**, 1012
[15] Couëdel L, Samarian A A, Mikikian M and Boufendi L 2008 *Phys. Plasmas* **15** 063705
[16] Childs M A and Gallagher A 2000 *J. Appl. Phys*. **87** 1086
[17] Denysenko I *et al* 2011 *J. Phys. D: Appl. Phys.* **44** 205204
[18] Denysenko I B *et al* 2013 *Phys. Rev. E* **88** 023104
[19] Berndt J, Kovacević E, Selenin V, Stefanović I and Winter J 2006 *Plasma Sources Sci. Technol.* **15** 18
[20] Stefanović I, Sadeghi N, Winter J and Sikimić B 2017 *Plasma Sources Sci. Technol.* **26** 065014
[21] Denysenko I B *et al* 2021 *J. Phys. D: Appl. Phys.* **54** 065202
[22] Denysenko I B *et al* 2018 *Phys. Plasmas* **25** 013703
[23] van Minderhout B, Peijnenburg T, Blom P, Vogels J M, Kroesen G M W and Beckers J 2019 *J. Phys. D: Appl. Phys.* **52** 32LT03
[24] Schweigert I V and Alexandrov A L 2012 *J. Phys. D: Appl. Phys.* **45** 325201
[25] Kravchenko O Yu, Maruschak I S and Yushchyshena Yu V 2015 *Probl. At. Sci. Technol.* **21** 220
[26] Agarwal P and Girshick S L 2012 *Plasma Sources Sci. Technol*. **21** 055023
[27] Babaeva N. Yu and Lee J. K. 2004 *IEEE Trans. Plasma Sci*. **32** 823
[28] Babaeva N Yu, Lee J K and Kim H C 2004 *Plasma Sources Sci. Technol*. **13** 127
[29] Economou D J 2014 *J. Phys. D: Appl. Phys.* **47** 303001
[30] Samukawa S and Mieno T 1996 *Plasma Sources Sci. Technol.***5** 132
[31] Lieberman M A and Lichtenberg M A 2005 *Principle of Plasma Discharges and Material Processing*, 2 nd ed. (New Jersey: JohnWiley & Sons Inc)
[32] Brown S C 1966 *Introduction to Electrical Discharges in Gases* (New York: Wiley)
[33] Stewart R A, Vitello P, Graves D B, Jaeger E F and Berry L A1995 *Plasma Sources Sci. Technol*. **4** 36
[34] Gerber R A and Gerardo J B 1973 *Phys. Rev. A* **7** 781

[35] Phelps A V 1990 *J. Res. Natl. Inst. Stand. Technol.* **95** 407, and references therein.
[36] Chantry P J 1987 *J. Appl. Phys.* **62** 1141
[37] Platier B, Limpens R, Lassise A C, Staps T J, Van Ninhuijs M A, Daamen K A, Luiten O J, Ijzerman W L and Beckers J 2020 *Appl. Phys. Lett*. **116** 103703
[38] Freiberg R J and Weaver L A 1968 *Phys. Rev.* **170** 336
[39] Hjartarson A T, Thorsteinsson E G and Gudmundsson J T 2010 *Plasma Sources Sci. Technol.* **19** 065008
[40] Kaganovich I D, Ramamurthi B N and Economou D J 2001 *Phys. Rev. E* **64** 03640
[41] Smith D, Dean A G and Adams N G 1974 *J. Phys. D: Appl. Phys.* **7** 1944
[42] Phelps A V and Petrovic Z L 1999 *Plasma Sources Sci. Technol*. **8** R21
[43] Allen J E 1992 *Phys. Scr.* **45** 497
[44] Khrapak S A *et al* 2013 *Phys Rev E* **87** 063109
[45] Goedheer W, Land V and Venema J 2009 Contrib. *Plasma Phys.* **49** 199
[46] Schwabe M and Graves D B 2013 *Phys Rev E* **88** 023101
[47] Khrapak S A, Ivlev A V, Morfill G E and Thomas H M 2002 *Phys. Rev. E* **66**, 046414
[48] Ivlev A V, Zhdanov S K, Khrapak S A and Morfill G E 2004 *Plasma Phys. Control. Fusion* **46**, B267
[49] Hutchinson I H 2006 *Plasma Phys. Control. Fusion* **48**, 185
[50] Kilgore M D, Daugherty J E, Porteous R K and Graves D B 1993 *J. Appl. Phys*. **73** 7195
[51] Epstein P S 1923 *Phys. Rev.* **23** 710
[52] Perrin J, Molinas-Mata P and Belenguer Ph 1994 *J. Phys. D: Appl. Phys.* **27** 2499
[53] Daugherty J E and Graves D B 1995 *J. Appl. Phys.* **78** 2279
[54] Byrne G D and Thompson S 2013 VODE_F90 support page (https://www.radford.edu/~thompson/vodef90web)
[55] Cui C and Goree J 1994 *IEEE Trans. Plasma Sci*. **22** 151
[56] Matsoukas T and Russell M 1995 J. Appl. Phys. **77** 4285
[57] Kang N, Oh S and Ricard A 2008 *J. Phys. D: Appl. Phys.* **41** 155203
[58] Liu F X, Guo X M and Pu Y K 2015 *Plasma Sources Sci. Technol.* **24** 034013
[59] Liu F X, Guo X M and Pu Y K 2015 *Plasma Sources Sci. Technol.* **24** 034013
[60] Gudmundsson J T 2001 *Plasma Sources Sci. Technol.* **10** 76
[61] Khrapak S A *et al* 2005 *Phys. Rev. E* **72** 016406
[62] Bouchoule A (ed) 1999 *Dusty Plasmas: Physics, Chemistry, and Technological Impacts in Plasma Processing* (New York: Wiley)
[63] Morfill G E, Tsytovich V N and Thomas H 2003 *Plasma Phys. Rep.* **29** 1
[64] Piel A and Melzer A 2002 *Plasma Phys. Control. Fusion* **44** R1
[65] Layden B, Couëdel L, Samarian A A and Boufendi L 2011 *IEEE Trans. Plasma Sci*. **39** 2764
[66] Wörner L *et al* 2013 *Phys. Plasmas* **20** 123702
[67] Chaubey N, Goree J, Lanham S J and Kushner M J 2021 *Phys. Plasmas* **28** 103702
[68] Biberman L M, Vorob'ev V S and Yakubov I T 1982/1987 *Kinetics of Nonequilibrium Low-Temperature Plasmas* (Moscow: Nauka, 1982; New York: Consultants Bureau, 1987)
[69] Yanguas-Gil A, Cotrino J and González-Elipe A R 2005 *Phys. Rev. E* **72** 016401
[70] Proshina O V, Rakhimova T V, Kovalev A S, Vasilieva A N, Zotovich A I, Zyryanov S M and Rakhimov A T 2020 *Plasma Sources Sci. Technol.* **29** 015015
[71] Gorchakov S, Loffhagen D and Uhrlandt D 2006 *Phys. Rev. E* **74** 066401
[72] Trunec D, Španěl P and Smith D 1994 *Contrib. Plasma Phys.* **34** 69